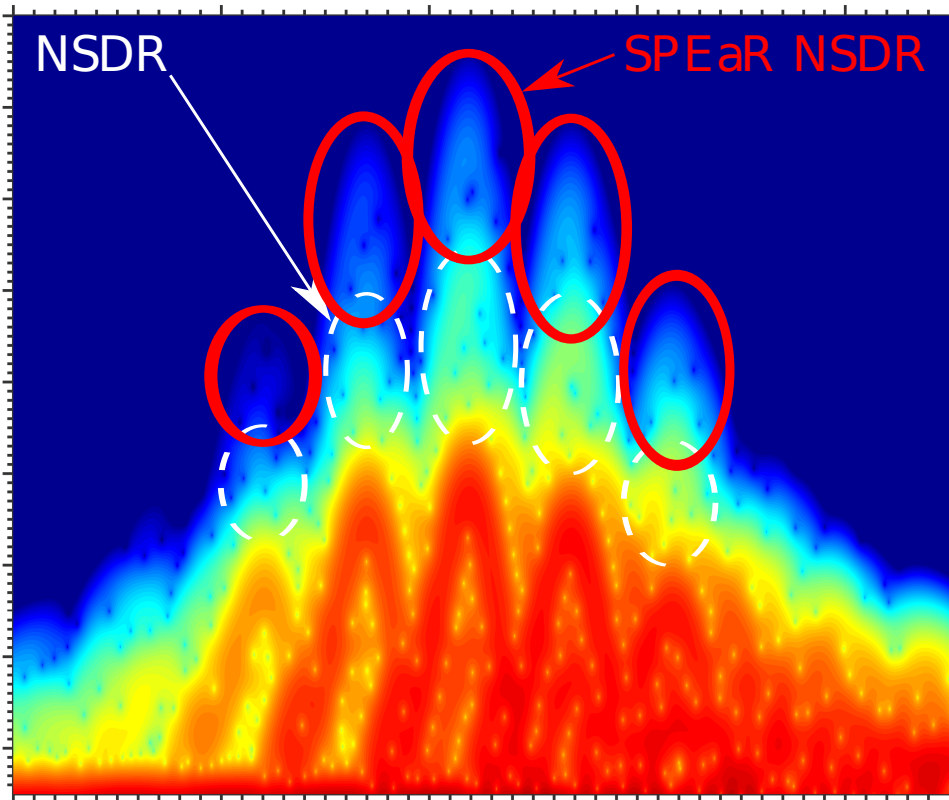


Two-Electron Correlation Effects in High Harmonic Generation



Kenneth K. Hansen

A progress report submitted for the qualifying exam
at the
Department of Physics and Astronomy,
Aarhus University

Supervisor: Lars Bojer Madsen
September 2016

Preface

This progress report is submitted for my qualifying exam at Aarhus University. This report presents the work I have performed in the past two years where chapter 4 is a slightly modified version of a paper published as part of the work [1]. As part of this work expansive models have been produced and used in conjunction with numerical calculations to study two-electron correlation effects in high harmonic generation. This is presented in chapter 2, 5 and 6. Finally the report concludes with an outlook for future subjects of study and a study abroad.

Contents

1	Introduction	1
2	Classical Analysis of High Harmonic Generation for One and Two Electrons	3
3	Solving the Time-Dependent Schrödinger Equation	8
4	Same Period Emission and Recombination Non-Sequential Double Recombination High Harmonic Generation	11
4.1	General Conclusions for Non-Sequential Double Recombination in Molecular-like systems	14
5	Molecular Non-Sequential Double Recombination High Harmonic Generation	15
5.1	Summary	19
6	Attosecond Pulse Enhancement of Non-sequential Double Recombination High Harmonic Generation	20
6.1	Further Study	21
7	Outlook	22
	Bibliography	23

1 Introduction

Attosecond- and femtosecond physics is the study of electrons on their natural time-scale of femtoseconds (10^{-15} s) and attoseconds (10^{-18} s).

This field of physics has been opened over the last three decades by the development of new lasers with previously unobtainable peak intensities. These intensities are strong enough to rival the Coulomb interaction resulting in extremely non-perturbative interactions between light and atoms or molecules enabling the study of new phenomenon like high harmonic generation (HHG) and non-sequential double ionization (NSDI) [2, 3, 4, 5]. The versatility of these new lasers only grow as the frequency range of the lasers available becomes larger for each passing decade [6]. Even in the coming decades the improvements on lasers continue with new sources being developed and large projects like the Extreme Light Infrastructure promising intensities of up to 10^{23}W/cm^2 or equivalently electric fields of up to 10^4 atomic units (a.u.) (Atomic units are used throughout the report unless indicated otherwise)[7].

These experimental tools allow for advanced control and measurement of strong field processes not previously possible. For strong fields the dominating processes are ionization of atoms and molecules and electron recombination or recollision of electrons with nuclei. Using these processes we can craft methods like attosecond streaking, reconstruction of attosecond beating by interference of two-photon transition (RABBIT) and light induced electron diffraction (LIED) to study physical systems [8, 9]. All of these methods use either emitted electrons or HHG to study systems and dynamics not possible by other means. Some methods also make use of the attosecond pulses. These pulses have durations so short that they can seem instantaneous even for electronic motion leading to these pulses being a precision tool able to choose distinct physical processes as seen later in the report in chapter 6.

Ionization of atoms and molecules is also of interest in of itself. Different dynamics for different fields and systems leads to interesting results about the systems themselves. In the following we will mainly use pulse parameters that put us in the tunneling regime of ionization and not focus on the emission process itself. A process originating from electrons emitted through ionization is HHG. The electron is emitted through either tunneling or multiphoton ionization into an electric field that moves the electron. The oscillating nature of light results in certain electron paths returning to the point of emission allowing for recombination. Through recombination a single photon is emitted with the total kinetic energy, K , the electron obtained in the field and the ionization energy, I_p , of the electron.

Through the emergence of these intense laser pulses, HHG has arisen as both a method of creating ultra-short pulses and as a tool to probe electron dynamics in atomic and molecular systems [8, 10, 11]. Using a many-cycle pulse of linearly polarized light HHG cutoff energies of $I_p + 3.17U_p$ have been found for one-electron dynamics where $U_p = I/(4\omega^2)$ is the ponderomotive potential with I the laser intensity and ω the angular frequency [12, 3, 4].

Molecular HHG spectra has been used to find a characteristic two-center interference minimum [13], and to control of alignment of the molecular axis with respect to the polarization of the driving field leads to harmonics of non-linear ellipticity [14, 15]. In relation to the work presented in this report, which will

focus on a unique molecular two-electron mechanism with distinctive cutoffs, we mention that for very large internuclear distances cutoffs in the HHG spectra emerge from the propagation of a single electron directly from one nuclei to another leading to kinetic energies up to $8U_p$ [16, 17].

Recently a two-electron HHG process was reported for an atomic system [18]. This non-sequential double recombination (NSDR) HHG process results in a new plateau in the HHG spectrum reaching beyond the one-electron HHG signal. NSDR was explained as two electrons propagating independently of each other in the field and then returning at the same instant to emit the combined kinetic energy of the two electrons as HHG. It was found that because electrons emitted in the same half-period of the field would have to propagate the same path to return at the same instant, electron-electron repulsion would make such a same-period emission process highly unlikely in the atomic case. Instead, only electrons emitted in different half-periods of the pulse could return at the same instant without electron-electron repulsion suppressing the process. Such electrons emitted in different periods traverse the nuclei more than once and can reach combined maximum return kinetic energies of $5.55U_p = 3.17U_p + 2.38U_p$ and $4.70U_p = 3.17U_p + 1.53U_p$ for first and third electronic return combined and first and second electronic return combined, respectively.

The work presented in this progress report has revolved around studying this two-electron effect in molecular-like systems. The two-electron nature of the process creates an opportunity for new effects not possible for one-electron HHG. The hope is to reach a better understanding of the NSDR HHG process and find interesting results for the molecular case not seen in the previously studied case of the atomic system. We also expand our analysis to the use of attosecond pulses to further our understanding of the process and make it a more viable for use in an experimental setting.

In chapter 2 we first present a classical perspective on the HHG process for both atomic and molecular systems. In chapter 3 we present the numerical tools and methods used to do time-dependent quantum calculations and in chapter 4 we present the first results for NSDR HHG in molecular systems obtained using these tools. In chapter 5 we present NSDR HHG for molecular systems and conclusions we have obtained using our classical models. In chapter 6 we present preliminary results obtained by using attosecond pulses to further test the results obtained in chapter 5 and improve the experimental viability of actually measuring NSDR HHG. Finally in chapter 7 we conclude on the obtained results and present where the work could be focused in the future and the possibility of a study abroad.

2 Classical Analysis of High Harmonic Generation for One and Two Electrons

Early theoretical work explaining the experimentally found HHG spectra found that a simple classical three-step model was able to explain the cutoff frequency of the photons detected from HHG [3, 4]. The success of such a classical model in describing a quantum mechanical effect comes from the partly classical nature of the process of HHG. The 3-step model of HHG explains the HHG process as such: Firstly the electron is emitted because of an electric field, this is the ionization step, the electron then propagates in the field and finally the electron recollides/recombines with an atom or molecule and emits the surplus kinetic energy and binding energy as a single photon with energy $\Omega = I_p + K$, where I_p is the ionization potential of the electron and K is the kinetic energy of the electron.

The following analysis will be independent on pulse frequency and amplitude and only depend on pulse envelope effects and will partly follow the analysis in reference [18]. Consider a homonuclear model H_2 molecule. We consider the co-linear case with the molecular axis parallel with the polarization of the field. A given pulse form can be analytically integrated and an expression for the position can be found. Practically this model is used by calculating the kinetic energy of the returning electron for all emission times in a model where all specifics of the ionization process and interplay with the nucleus(nuclei) is ignored. Assume the electron is released in the continuum at time t_i , at position $x = 0$ with zero momentum. The electron then propagates in the external field with momentum $\mathbf{p}(t) = \mathbf{A}(t) - \mathbf{A}(t_i)$ and position given as $\mathbf{r}(t) = \boldsymbol{\alpha}(t) - \boldsymbol{\alpha}(t_i) - \mathbf{A}(t_i)(t - t_i)$ where $\mathbf{A}(t)$ is the vector potential of the field and $\boldsymbol{\alpha}(t) = \int_{t_i}^t dt' \mathbf{A}(t')$ is the quiver motion of the electron in the field. In general the vector potential can be written as $\mathbf{A}(t) = A_0 f(t) \sin(\omega t + \phi)$ where A_0 is the amplitude of the pulse, $f(t)$ is the envelope of pulse, ω is the frequency and ϕ is the phase. For a long pulse the phase ϕ will have no effect on the cutoff but for short pulses the cutoff will depend on the envelope $f(t)$ and the phase ϕ .

Solving these equations for $\mathbf{r}(t_r) = 0$ enables us to find the return kinetic energy of the electron for all emission times t_i . The return kinetic energy of electrons as a function of return time for a long pulse can be seen in Fig. 2.1 (a) and in Table 2.1. As will be seen later these cutoffs change when the model is expanded to include more physical effects and a more complicated pulse.

This simple model for one-electron HHG is expanded for NSDR HHG by adding up the energy each electron will have obtained in the field and ignoring any electron-electron interaction. With this the classical NSDR cutoff is expected at $\Omega \simeq N\omega = I_p^{(1)} + I_p^{(2)} + K_1(t_r) + K_2(t_r)$, where N is the harmonic order, ω is the driving frequency and $K_i(t_r)$ is the return energy of electron i at time t_r (see Fig. 2.1 (b)). The maximum return energy differs in each period and second and third return energies are strongly dependent on the shape of the envelope of the short pulse as seen in Fig. 2.1 (a). The NSDR HHG cutoffs can be seen in table 2.1. In the atomic case it is expected that the main part of the NSDR signal comes from recombination of electrons ionized in different cycles of the pulse as electrons ejected in the same cycle repel each other and make NSDR very unlikely. Electrons ejected in different cycles of the pulse do not interact much and the electron-electron repulsion is therefore ignored in all cases.

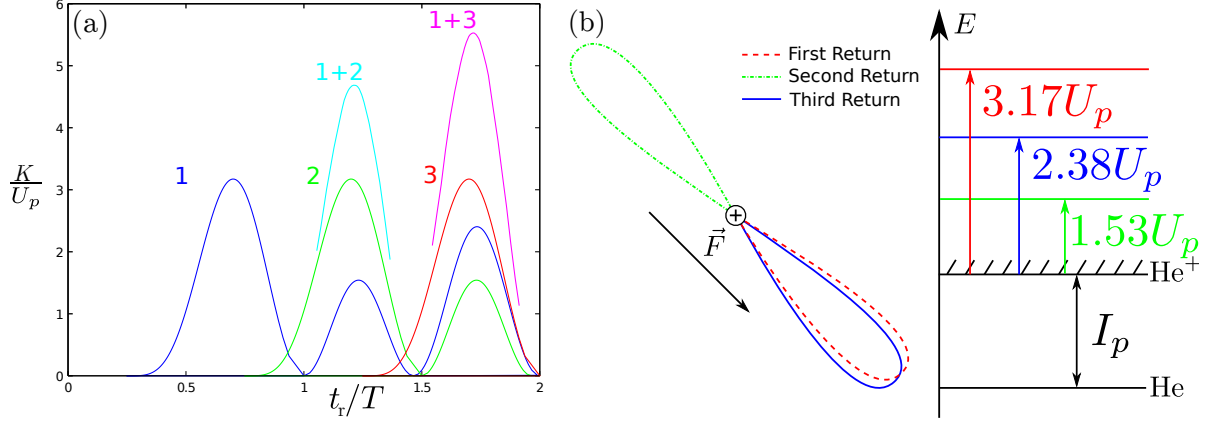


Figure 2.1: The classical cutoffs for electrons returning for the first, second and third time in a pulse without envelope effects. Fig. (a) shows the electron return kinetic energy as a function of return time in units of the period of the field for first (1) second (2) and third (3) return as the blue graph. The green and red graph are references for electrons emitted in the following periods. The NSDR return kinetic energies are shown as "1+2" and "1+3" as a first and second time returning electron combined and a first and third time returning electron combined. Fig. (b) shows the cutoff energies for the returning electrons. The first return gives $3.17U_p + I_p$, the second gives $1.53U_p + I_p$ and the third gives $2.38U_p + I_p$.

Table 2.1: Maximum electron return kinetic energies in units of U_p in the long pulse limit and for a 6-cycle pulse as describe in eq. 3.3 for one and two electrons. The left column denotes the number of electrons involved and the return events. These results were published by us in reference [1].

	long pulse	6-cycle pulse
one-electron, first return	3.17	3.08
one-electron, second return	1.53	1.61
one-electron, third return	2.38	2.15
two-electrons, first and second return	4.70	4.69
two-electrons, first and third return	5.55	5.23
two-electrons, first and first return	6.34	6.16

When considering a short pulse as used in this work the cutoff energies change, we have therefore also calculated them for a 6-cycle pulse as described in Eq. 3.3. The results obtained for Helium ($R = 0$) are shown in Fig. 2.2. In Fig. 2.2 electrons emitted in the same half-period of the electric field are grouped for all return times and the NSDR signals are shown by black solid curves. The NSDR energies are calculated by adding the first return energies with the 2nd, 3rd, etc. return energies. The pulse envelope shape is reflected in the return energies K . The 6-cycle pulse used has one dominant period where the single electron cutoff for return is $3.08U_p$ seen at the top of the middle dashed (blue) curve in Fig. 2.2. The deviation from the long-pulse result $3.17U_p$ is due to the consideration of the pulse envelope and phase. Quantum mechanical the probability of an electron returning a third time is significantly smaller than the probability of an electron returning for a second time. It is therefore expected that the NSDR cutoff from one electron returning for the first time and the other returning for a second time for a combined kinetic energy of $4.69U_p = 3.08U_p + 1.61U_p$ will be clearly present even though an electron returning for the first time and the other returning for the third time has a higher energy of $5.23U_p$. It will later be seen that this indeed is the case.

Molecular effects are introduced by considering the nuclei at which emission and recombination happen as illustrated in Fig. 2.4. For the atomic case both emission and recombination is expected at the

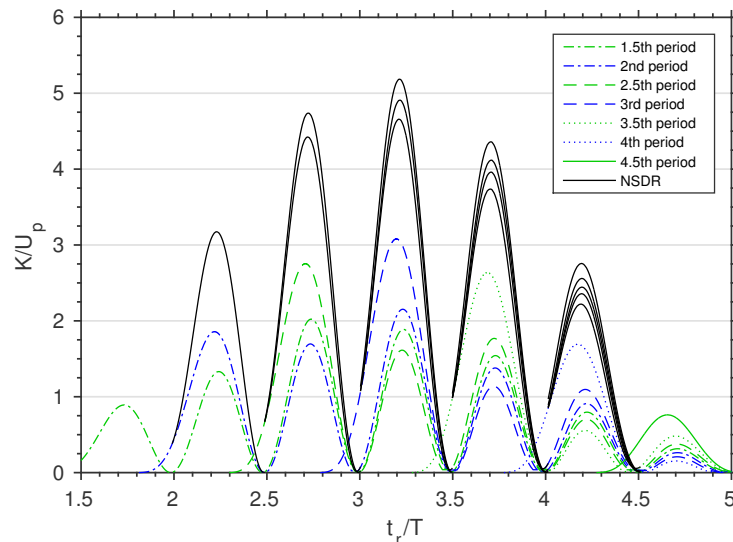


Figure 2.2: One- and two- electron return kinetic energies K in units of U_p predicted from a classical model with a 6-cycle pulse as a function of return time t_r in units of the laser cycle period T . One-electron return energies are shown as lower (blue and green) curves and are grouped according to which half-cycle of the electric field the electrons originate from. The dashed (blue) curves are electrons emitted in the 3rd period of the pulse returning to the nuclei at all times from $2.8T$ and in all subsequent periods of the pulse with a maximum return energy of $3.08U_p$. Above the one-electron energies are electron return energies from different periods added together to predict the NSDR energies (black curves). Only the first of the returns of electrons are added with 2nd, 3rd, etc. returns as other combinations will be unlikely (see text).

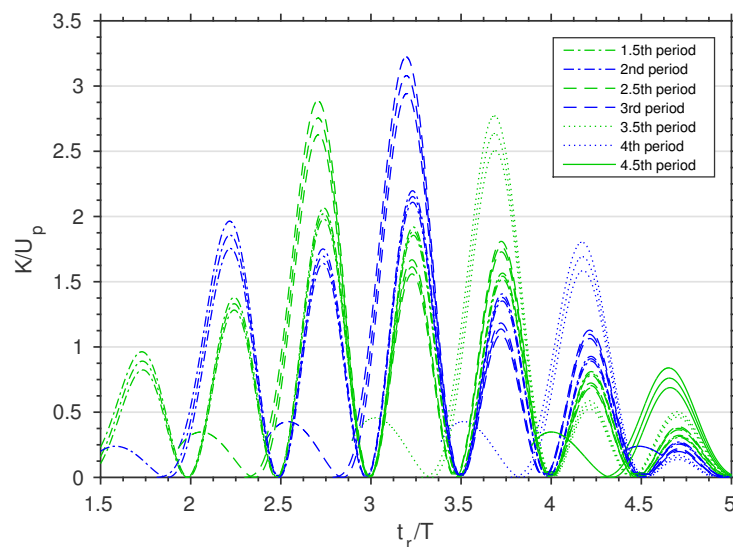


Figure 2.3: Classical HHG return kinetic energies K in units of U_p for paths with different electron emission times for H_2 with $R = 4$ interacting with a 6-cycle pulse as a function of return time t_r in units of the laser cycle period T . The small difference in path lengths for the different direct and exchange paths possible in molecules, as illustrated in Fig. 2.4, creates a spread in return energies. This can be seen clearly at the top of the highest peak originating from the 3rd period of the electric field; all three curves show return energies for electrons emitted in the same half period of the electric field but because of the difference between direct paths and long and short exchange paths there will be three distinct classical return energies. Direct exchange paths from one nuclei to the other can be seen as small peaks with a maximum at $K \simeq 0.5U_p$ out of phase with the other larger peaks. Such paths can be seen at the foot of the highest peak originating from the 3rd period of the electric field where one curve starts before the other two with an extra peak being emission at one nuclei and propagation directly to the other nuclei for recombination.

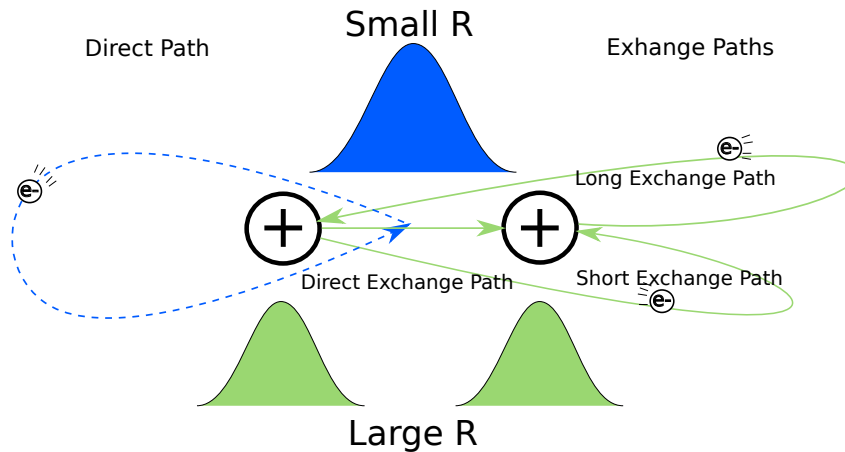


Figure 2.4: Illustration of direct and exchange paths for a diatomic molecule. For a small intermolecular distance the ground state wave function (top Gaussian-like, blue) is localized between the nuclei and no exchange paths will be relevant. For larger intermolecular distances (bottom Gaussian-like, green) the ground state wave function is localized on each nuclei and an electron can therefore be emitted at one nuclei and recombine at the other. There are three exchange paths: Long exchange paths where the electron gains an additional propagation length of R by not recombining at the nuclei of emission and instead recombining at the other nuclei further away, short exchange paths where the electron recombines at first nuclei reached in the propagation thereby shortening the propagation length by R and direct exchange paths where the electron propagates directly to the other nuclei to recombine.

nuclei, i.e., at $\mathbf{r}(t_i) = \mathbf{r}(t_r) = 0$. In the molecular case emission and recombination at the nuclei would be expected for molecules where the ground state electron density is centered at these points. This would also introduce recombination at a different nuclei than emission as seen in Fig. 2.4 for long exchange paths, short exchange paths and direct exchange paths respectively. These exchange paths with a different nuclei for recombination than emission will be energetically different from the atomic case and therefore of interest in identifying molecular effects.

The single electron classical return energies for the molecular case are shown in Fig. 2.3 for our aligned H_2 model with an intermolecular distance $R = 4$. In the molecular case exchange paths are considered (Fig. 2.4) which result in extra HHG return kinetic energies at each return time t_r for each period. These extra return kinetic energies can be seen as the extra curves in Fig. 2.3 when compared with Fig. 2.2. The curves are similar to the atomic case as the paths are similar to the atomic case for the relatively small intermolecular distance used. The exchange paths create a spread in return energies and this spread grows for larger intermolecular distances. The cutoff for long, short and direct exchange paths for the 6-cycle pulse and for a long pulse can be seen in Fig. 2.5. The return energies for the different exchange paths depend on the difference between the quiver length $\alpha_0 = A_0/\omega$ and R as seen in Fig. 2.5. The closer α_0 and R , the bigger the difference from the atomic kinetic return energy of $3.08U_p$ for the 6-cycle pulse or $3.17U_p$ for the long pulse limit. The molecular exchange paths are expected to be predominantly seen for molecules where the electronic ground-state is located at each nuclei which would be the case for large-intermolecular-distance H_2 (as explained in Fig. 2.4). Direct exchange paths are also seen for the molecular case in Fig. 2.3. These paths result in the small out-of-phase peaks with a maximum of approximately $K = 0.5U_p$ (see discussion in caption of Fig. 2.3). These also become more pronounced when R is comparable with α_0 as seen in Fig. 2.5.

Previously in the literature other cutoffs have been found for HHG in molecular systems. For large intermolecular distances the direct exchange path was shown to have a cutoff of $8U_p$ and back scattering

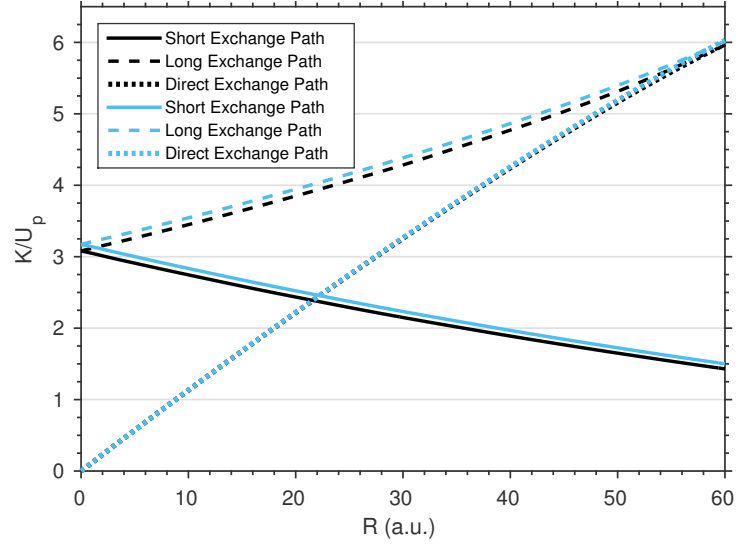


Figure 2.5: The kinetic return energies K in units of U_p obtained by an electron propagating in the exchange paths presented in Fig. 2.4 as a function of the internuclear distance, R . The black curves show results for a 6-cycle pulse and the blue curves show results for the long pulse limit.

reaching up to $32U_p$ [16, 17]. These cutoffs will only be relevant when the intermolecular distance is of the same size as the maximum propagation length in one half cycle of the pulse, which is not the regime of interest in the current analysis.

All of these calculations assume the electrons are emitted on the nuclei and appear with zero momentum, things which are known not to be true for tunneling ionization [19]. Other effects will also be seen later to be of importance for NSDR but without data to compare the models with all such considerations are impossible to prioritize. We therefore have to do quantum calculations of the process. These calculations have to be done with full electron-electron correlation creating complications that will be considered in chapter 3.

3 Solving the Time-Dependent Schrödinger Equation

Several techniques have been developed over the last couple of decades to help tackle problems in ultrafast physics. Extremely successful techniques like the strong field approximation (SFA) or its evolutions has shown themselves capable of solving problems with a strong intrinsic capability to analyze the results with meaningful physical interpretations [20]. But for advanced systems and processes like NSDR HHG where it will be shown that several interactions interplay in the process, such methods become unproductive and solving the time-dependent Schrödinger equation (TDSE) becomes the best option to solve and analyze such advanced processes. Even when SFA is an option it is always preferable to have ab-initio TDSE solutions of the problem or a reduced dimensionality model solution if ab-initio is not computationally possible.

Solving the TDSE can be done with a variety of different approaches. Depending on the problem different approaches will be preferable or in some cases be the only option because of the specifics of the problem. For molecules schemes like Coupled Cluster (CC) or Configuration Interaction (CI) has shown themselves to be effective; for electron dynamics methods like time-dependent restricted-active-space self-consistent-field (TD-RASSCF) developed in our own group to solve specific problems not possible to be solves with other methods [21, 22].

For the specific problem of NSDR HHG we have chosen the split-step operator Crank-Nicolson (Peaceman-Rachford) method as in Ref. [18, 23]. We have also tried a split-step Fourier method but it was not able to obtain the sensitivity needed to model NSDR HHG. The Crank-Nicolson methods makes no assumptions about the system and enables us to use full electron-electron correlation which is necessary when modeling NSDR HHG.

The TDSE calculations are made using a co-linear model for H_2 , where the nuclei are fixed and the electrons move in one spatial dimension. The reduced dimensionality of the system is necessary for it to be computationally possible to solve. Because of the reduced dimensionality the Coulomb interactions have to be modified to remove the singularity as it is not possible to handle in one dimension. This modification is done by introducing a softening factor in the denominator of the Coulomb potential, removing the singularity. The Hamiltonian then reads

$$H(t) = \sum_{i=1}^2 \left(\frac{[p_i + A(t)]^2}{2} + V_R(x_i) \right) + W(x_1 - x_2), \quad (3.1)$$

with p_i the canonical momentum, $A(t)$ the vector potential, $V_R(x_i) = -Z((R/2 - x_i)^2 + \epsilon_{ei})^{-1/2} - Z((R/2 + x_i)^2 + \epsilon_{ei})^{-1/2}$ the Coulomb interaction with the nuclei, Z the nuclear charge, R the intermolecular distance, x_i the position of electron i and $W(x_1 - x_2) = ((x_1 - x_2)^2 + \epsilon_{ee})^{-1/2}$ the electron-electron interaction. Our model He system is obtained by setting $R = 0$ in the above. We use the vector potential of the field and solve the TDSE in velocity gauge. The softcore parameters were set to $\epsilon_{ei} = 0.5$ and $\epsilon_{ee} = 0.329$ corresponding to $I_p^{(1)} = 0.9$ and $I_p^{(2)} = 2.0$ for ionization of respectively the first and second electron in He. We keep the softening parameters fixed in all calculations. For $R = 16$, e.g., the ionization potential is $I_p^{(1)} = 0.95$ and $I_p^{(2)} = 0.89$.

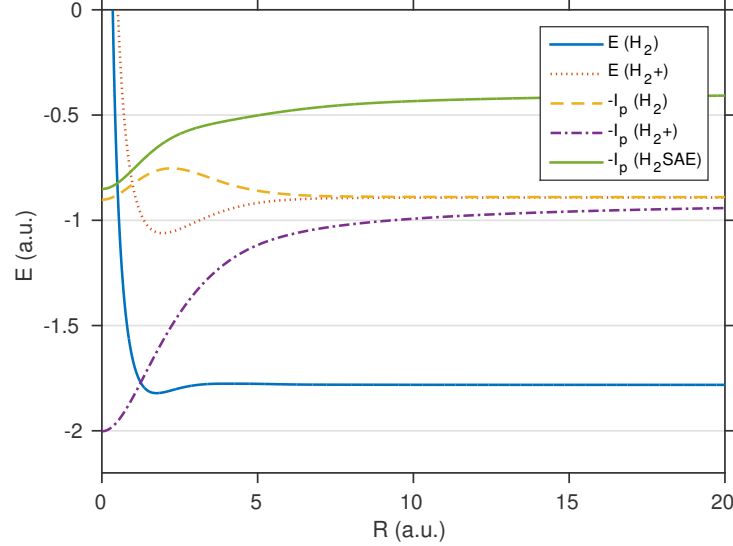


Figure 3.1: Born-Oppenheimer energy curve for H_2 [$E(H_2)$] and H_2^+ [$E(H_2^+)$] for $R \in [0; 20.0]$. Also shown are the negative ionization potentials for H_2 , H_2^+ and $H_2(\text{SAE})$.

Ground states and their energies are found by imaginary time-propagation with a time step of $\Delta t = 0.15$ and a Born-Oppenheimer potential energy curve for H_2 and H_2^+ for $R \in [0, 14]$ are shown in Fig. 3.1. The grid step size and real time-propagation step size depends on the pulse parameters used. The grid step-size is determined so it is able to handle the maximum momentum expected to be simulated, $\Delta x < 1/p_{max}$. In the case of HHG, electron re-collision with the nuclei or very large molecules can lead to electron kinetic energies of $K_{max} = 10U_p$ or $\Delta x = 1/\sqrt{2 \cdot 10U_p}$. We use $12U_p$ to have room for error. The real time-propagation step is approximated so that the exponential propagation operator used in the calculations is less than unity, $E_{max}\Delta t \ll 1$. The maximum energy obtainable in the HHG process is $E_{max} = I_p^{(1)} + I_p^{(2)} + 10U_p$, where in our case two electrons can recombine at the same time leading to two ionization potential contributions. We therefore choose $\Delta t = 1/(I_p^{(1)} + I_p^{(2)} + 15U_p)$ again to have room for error. These step sizes have been confirmed with convergence of the results of the imaginary time-propagation and real time-propagation. In the real time propagation a complex absorbing potential (CAP), of the form

$$V_{\text{CAP}} = 50 \left| \frac{x_i}{L/2} \right|^{16}, \quad (3.2)$$

where L is box size, was used. The box size of the calculation is determined by the size of the quiver motion, α , for the specific pulse used. We are only interested in electrons able to return to the nuclei which classically is true for $|x| < 2\alpha$. Since any reflection on the CAP could introduce noise that drowns the relatively weak two-electron HHG signal a conservative box size of $L = 8\alpha$ is chosen.

Several different pulse types are used in our calculations. Short pulses used have the form

$$A(t) = \frac{F_0}{\omega} \sin^2 \left(\frac{\omega t}{2n} \right) \sin(\omega t), \quad 0 \leq t \leq T_n \quad (3.3)$$

with typically 6-cycles ($n = 6$), $\omega = 0.0584$ ($\lambda \simeq 780$ nm), $F_0 = 0.119$ ($I \simeq 5.0 \times 10^{14}$ W/cm²) and

the pulse polarization is linear and parallel with the molecular axis. Long pulses used have the form

$$A(t) = \begin{cases} F_0/\omega \sin(\omega t) \sin^2\left(\frac{\pi}{2}\frac{t}{T_u}\right) & 0 < t < T_u \\ F_0/\omega \sin(\omega t) & T_u < t < T_{u+n} \\ F_0/\omega \sin(\omega t) \cos^2\left(\frac{\pi}{2}\frac{t-T_u-T_k}{2T_u+T_n}\right) & T_{u+n} < t < T_{2u+n} \end{cases} \quad (3.4)$$

where $T_u = 2\pi m/\omega$ with $m = 3$, $T_n = 2\pi n/\omega$ with n describing the length of the pulse where typically $n = 15$. Both pulse types are used as the short pulses are faster to calculate but the long pulses have simpler interpretations classically, as will be seen later in chapter 4 and 5.

In the TDSE calculations the observable of interest for the HHG spectrum is the dipole acceleration. The dipole acceleration has advantages to the direct dipole as it ignores contributions from ionized electron [24, 25]. The harmonic spectrum is calculated by taking the modulus square of the Fourier transformed dipole acceleration, $a_{dip}(t)$, which is calculated in every time-step as

$$a_{dip}(t) \equiv \frac{d^2}{dt^2} \langle x_1 + x_2 \rangle \quad (3.5)$$

$$= \langle \psi(t) | -\nabla_{x_1} V(x_1, x_2) - \nabla_{x_2} V(x_1, x_2) | \psi(t) \rangle, \quad (3.6)$$

where ∇_{x_i} is the gradient with respect to coordinate x_i ($i = 1, 2$) and $\psi(t)$ is the electronic wave function at time t . In Eq. 3.6 the electric field is omitted since it would only contribute to the spectrum at the order of ω [24]. A window function of the Nuttall-type was used when performing the Fourier transform [26]. This is necessary to reduce the "leakage" of the main low frequency contributions to the HHG signal into the higher frequency signals with much lower amplitude after performing the Fourier transform.

A time-frequency analysis is also performed on the dipole acceleration expectation value. This is done with a short-time Fourier transform (Gabor Transform) of the dipole acceleration expectation value:

$$\tilde{a}_{dip}(\Omega, t) = \int_{-\infty}^{\infty} dt' e^{-i\Omega t'} a_{dip}(t) e^{-4 \ln(2)(t'-t)^2/\text{FWHM}^2}, \quad (3.7)$$

where FWHM is the full-width-half-maximum duration of the Gaussian window function which is set to $0.1 \times 2\pi/\Omega$. This width produces clear plots. When using a small window as used here, the STFT goes to the classical limit enabling us to compare time dependent quantum mechanical results with time dependent classical results.

Single active electron (SAE) calculations on He and H₂ have also been done with frozen-core potentials. The potentials were created from ground state Hatree-Fock orbitals of He⁺ and H₂⁺, found via imaginary time propagation, resulting in an effective potential of the form

$$V(x) = \int dx' \frac{|\phi_0(x')|^2}{\sqrt{(x-x')^2 + \epsilon_{ee}}}, \quad (3.8)$$

where $\phi_0(x)$ is the ground state orbital of either He⁺ or H₂⁺.

Using these tools we are able to calculate the HHG spectrum for all internuclear distances for one- and two-electron systems. Combining these spectra and the classical models from chapter 2 we are able to identify new cutoffs and develop theory that explains the molecular effects arising in the molecular system.

4 Same Period Emission and Recombination Non-Sequential Double Recombination High Harmonic Generation

Using the computational methods described in chapter 3 we have used our co-linear model to perform calculations for many different internuclear distances in the interval $[0; 80]$. In these initial studies we detected a new signal not predicted in the previously studied atomic system. This new NSDR HHG signal was identified as a new molecular effect in NSDR HHG where the electrons undergo same period emission and recombination (SPEAR). We also established a new effect not previously studied in HHG where the electrons interact with bare nuclei because of the two electron nature of the process. The results presented in this chapter were published in [1].

Figure 4.1 shows the HHG spectra for our He model [Fig. 4.1(a)] and H_2 model [Fig. 4.1(b)] with internuclear distance $R = 16.0$ as a representative example. For the 6-cycle pulse, Fig. 4.1(a) shows the one-electron cutoff of $I_p^{(1)} + 3.08U_p$ and the atomic NSDR cutoffs $I_p^{(1)} + I_p^{(2)} + 4.69U_p$ and $I_p^{(1)} + I_p^{(2)} + 5.23U_p$ as described in chapter 2. Comparing the cutoffs in Figs. 4.1(a) and (b) a new cutoff can be seen in Fig. 4.1(b) at $\Omega \approx 145\omega$. Our extensive calculations for many internuclear distances show that this new cutoff emerges for internuclear distances of $R \gtrsim 8.0$, i.e., in the limit where the Born-Oppenheimer potential is relatively flat. In this limit, the two electrons are predominantly confined to separate nuclei and the electron-electron interaction is weak. When we increase R from $R = 0$ (He case) up to $R \simeq 8$, we observe a continuous change of the atomic-like NSDR signal. At $R = 8$, we see a pronounced build-up of the new signal seen in Fig. 4.1(b).

For the present laser parameters, the one-electron signal with a cutoff of up-to $8U_p$ and corresponding

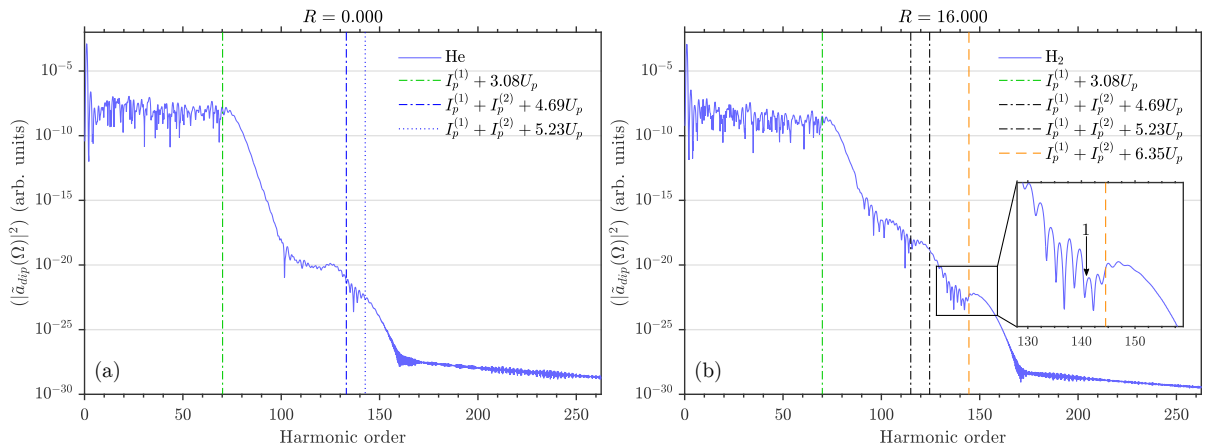


Figure 4.1: HHG spectra for (a) the He model and (b) the H_2 model with $R = 16.0$. The spectra are shown in units of the Harmonic order for an $n = 6$ -cycle laser pulse at $\omega = 0.0584$ ($\lambda \simeq 780$ nm) and $F_0 = 0.119$ ($I \simeq 5.0 \times 10^{14}$ W/cm²). The HHG cutoffs for one- and two electron HHG are shown as the dotted vertical lines at $I_p^{(1)} + 3.08U_p$, $I_p^{(1)} + I_p^{(2)} + 4.69U_p$ and $I_p^{(1)} + I_p^{(2)} + 5.23U_p$. In (b) the SPEAR NSDR HHG cutoff is shown as the dashed line at $I_p^{(1)} + I_p^{(2)} + 6.39U_p$. The insert in (b) shows a zoom-in of the SPEAR NSDR cutoff. The arrow at 1 is at $I_p^{(1)} + I_p^{(2)} + 6.16U_p$ (see text).

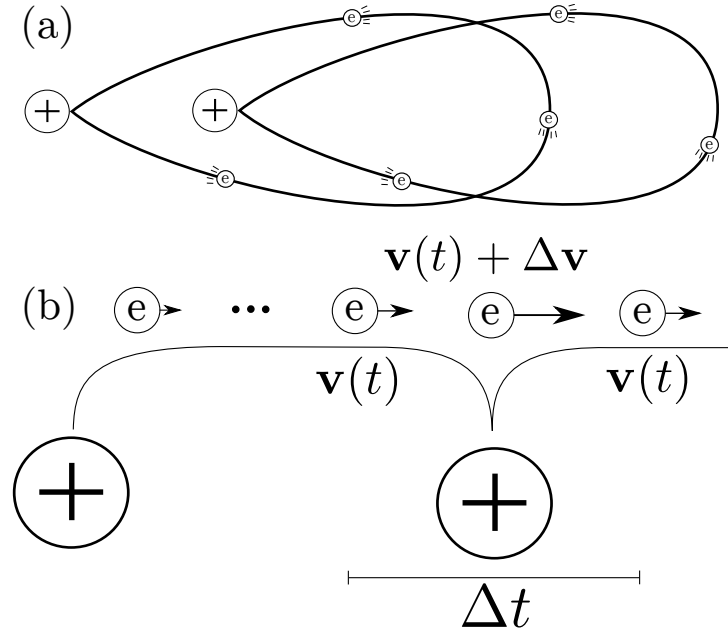


Figure 4.2: (a) Illustration of the mechanism responsible for SPEAR. At large intermolecular distances, $R \gtrsim 8$, electrons emitted at the same time at different nuclei will interact relatively weakly. Therefore both electrons are able to reach the maximum kinetic return energy of $3.08U_p$ in the considered pulse. (b) An electron emitted at one nuclei in NSDR (both electrons are in the continuum for NSDR) could traverse a bare nuclei and thereby obtain a velocity increase of $\Delta\mathbf{v}$ which leads to a longer path in the continuum of approximately $\Delta\mathbf{r} = \Delta\mathbf{v}\Delta t$. This increases the kinetic energy of the returning electron by an amount dependent on the intermolecular distance (See text).

to direct trajectories from one nuclei to another becomes dominant for $R \gtrsim 40.0$, and therefore the new signal is only observed for $R \in [8; 40]$. For these internuclear distances the cutoff is higher in energy than the atomic NSDR cutoff. Also the new cutoff does not have the distinct strong dependence on the internuclear distance expected for the one-electron high energy cutoff for large internuclear distances [16, 17]. We therefore conclude that it can not originate from earlier proposed one-electron or two-electron HHG mechanisms. Here we propose a unique molecular two-electron process of NSDR HHG to explain this new cutoff.

As the internuclear distance increases the assumption that electron-electron repulsion forbids electrons emitted in the same period from returning at the same instant and recombining as NSDR is no longer justified. For large R , the electron-electron repulsion plays a minor role even if the electrons are emitted at the same instant. Therefore they will be able to propagate approximately the same path as if they were emitted from an atomic system and return with the combined maximum return kinetic energy of $2 \times 3.08U_p = 6.16U_p$ for the 6-cycle pulse ($2 \times 3.17U_p = 6.34U_p$ in the long pulse limit) [see Table I]. This is same period emission and recombination NSDR (SPEaR NSDR) and the mechanism is illustrated in Fig. 4.2(a).

Because the molecule is oriented with the molecular axis parallel to the laser field polarization, the cutoff for SPEAR depends on the internuclear distance. While one electron after ionization is well described by taking into account only the interaction with the external field [the electron to the right in Fig. 4.2(a)], the other electron interacts with a bare nuclei as shown in Fig. 4.2(b) for high return kinetic energy paths. This Coulomb interaction modifies the electron propagation for one of the electrons, and enables an increase of the kinetic energy of the returning electron and makes the cutoff dependent on the

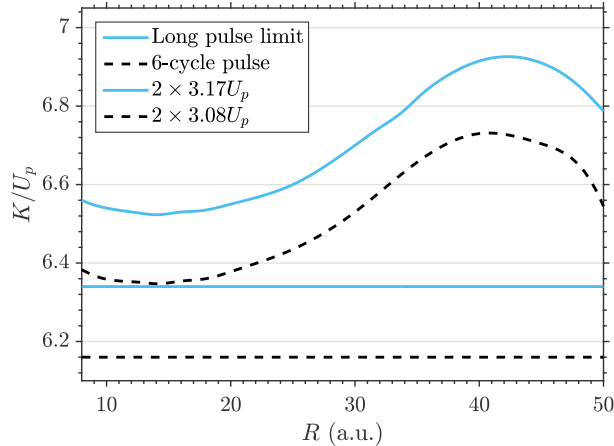


Figure 4.3: Classical SPEAR return kinetic energy K in units of U_p of one electron propagating in a laser field added to that of an electron propagating in a laser field and a Coulomb potential located at R with emission at $r(t_i) = 0$ as a function of the internuclear distance, R . Here the combined kinetic return energy of the two electrons is shown for the long pulse limit (upper solid curve) and for the 6-cycle pulse (upper dashed curve) and the expected SPEAR return kinetic energy without the modification introduced by the Coulomb potential for the long pulse limit (lower solid line) and the 6-cycle pulse (lower dashed line).

internuclear distance.

The SPEAR NSDR cutoff as a function of the internuclear distance is approximated by modeling a single electron propagating in the pulsed-field interacting with the Coulomb potential. The cutoff energy is then calculated by solving the classical equations of motion numerically and adding the atomic HHG cutoff energy to the maximum return kinetic energy of the modeled electron. The classical cutoff predicted by this model is found to fit for all calculations made in the range $R \in [8.0; 40.0]$ where the new signal is observed. As mentioned above, for $R \gtrsim 40.0$ the SPEAR NSDR HHG signal is not observed as the one-electron cutoff from direct paths becomes the dominant signal in that spectral range by several orders of magnitude. The difference between the simple model of the cutoff, $I_p^{(1)} + I_p^{(2)} + 6.16U_p$, [marked at 1 in Fig. 4.1 (b)] and the model with the Coulomb potential included, $I_p^{(1)} + I_p^{(2)} + 6.39U_p$, is highlighted in the insert in Fig. 4.1 (b). Though the difference is relatively small the inclusion of the Coulomb potential results in the classical prediction of the cutoff fitting perfectly for all internuclear distances that we have considered. This is in contrast to the simple model where the predicted cutoff is always shifted away from the observed cutoff. The cutoff as a function of the internuclear distance is shown in Fig. 4.3. The calculated cutoffs shown in Fig. 4.3 are, in contrast to the models in chapter 2, dependent on the pulse parameters as the specific excursion path and excursion length of the electron is dependent on the pulse parameters and the interaction is an interplay between the specific excursion path and excursion length of the electron and the internuclear distance. The structure in the calculated SPEAR NSDR cutoffs in Fig. 4.3 around $R \approx [40; 50]$ is due to this being the maximum propagation length for short HHG paths.

We also performed calculations in the long pulse limit and found that SPEAR NSDR HHG is still observed and that the classically predicted cutoff is correct.

To compare the classical model with the quantum mechanical results a short-time Fourier transform (STFT) (Gabor transform) of the dipole acceleration is performed. Figures 4.4(a) and (b) show the STFT of the dipole acceleration for our model He and H₂ for $R = 16.0$. The NSDR signal is marked with dashed circles in both figures and the SPEAR NSDR signal is marked with full circles in Fig. 4.4(b). The SPEAR NSDR is clearly located directly above the NSDR signal and not shifted to the left as would be

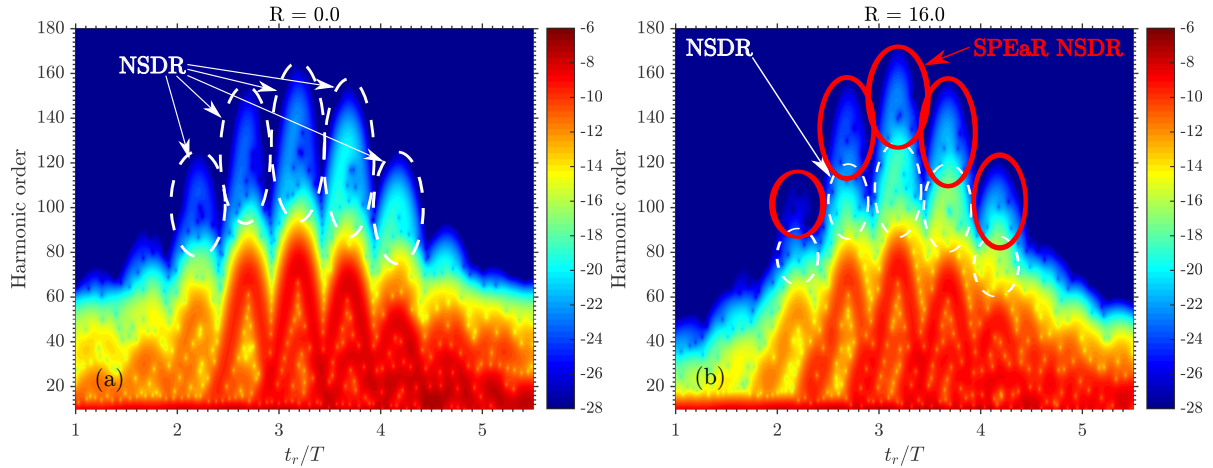


Figure 4.4: Norm square of the short-time Fourier transforms of the dipole acceleration of our model He and H₂ with $R=16.0$ on a logarithmic scale as a function of the return time t_r in units of the laser cycle period, T , and return energy in orders of the pulse center frequency ω . The NSDR signal is marked with dashed circles in (a) and (b). SPEAR NSDR HHG is marked with full circles in (b).

expected for the high energy cutoffs observed for large internuclear distances. This shift to the left is expected because the high energy cutoff for large internuclear distances originates from direct exchange paths where electrons propagate directly from one nuclei to the other. Therefore the recombination time will happen earlier than for electrons propagating out and returning again for recombination. The new signal is also seen directly above one-electron HHG which supports the conclusion that this new signal originates from a similar process to one-electron HHG and NSDR HHG where the electron propagates in the field and returns to the same nuclei after changing direction in the continuum, as described by the three-step-model. The SPEAR signal being above the one-electron HHG and NSDR HHG is also what is expected from the classical model and therefore the STFT results support the proposed model.

4.1 General Conclusions for Non-Sequential Double Recombination in Molecular-like systems

There is a clear effect of electrons interacting with bare nuclei as they propagate in the continuum in the SPEAR NSDR HHG signal but this effect should also be present in the atomic NSDR HHG signal and should be included in the full molecular model. The two-electron nature of the NSDR HHG process will always have an electron interacting with bare nuclei when propagating. This interaction will be dependent on the internuclear distance and will therefore be of relevance when comparing different molecular systems. A complication in using short pulses can also be seen in fig. 4.1 (a) when comparing the expected cutoffs in the atomic case with what is seen in the spectrum, they do not match well. The problem can be seen clearer in fig. 4.4 (a) where the signal is stronger in the period after the highest peak. This occurs because the ionization rate is a limiting factor for NSDR HHG in the strongly bound atomic system where the second electron has an ionization potential of 2 a.u. and therefore the period with the largest field strength will naturally lead to most ionization thereby raising the signal in the periods after. This problem is not observed for larger internuclear distances as the ionization potential is lowered but for simplicity when analyzing the system this problem can be counteracted by using long pulses instead of short pulses.

5 Molecular Non-Sequential Double Recombination High Harmonic Generation

Using the computational methods described in chapter 3 we have used our co-linear model to perform calculations for many different internuclear distances in the interval $[0; 80]$ now with the long pulse described in eq. 3.4 with $n = 15$. We found in chapter 4 that to describe the SPEAR NSDR HHG signal the classical model had to be expanded to include the interaction with the bare nuclei because of the two electron nature of the process leaving one nuclei bare after emission of an electron. This is not relevant for the one-electron signal as the only paths where such an interaction would be relevant are the paths passing the core multiple times, but these paths are not visible in the spectrum because of their low return energy (see fig. 2.1). The interaction with a bare nuclei is closely related to the time delays measured for photoionization as both are Wigner delays/phaseshifts from interacting with the Coulomb interaction [27]. The difference is that we have the full interaction but in photo ionization only have half as they start close to the center of the Coulomb interaction.

In the three step model we emit the electron at a nuclei with zero momentum to interact with the field and all interaction with the Coulomb potential from the nuclei is put into the ionization potential. This simplification of the interaction between the electron and the nuclei is of course an approximation that has previously shown itself to be valid for most cases through the success of the three step model but as shown in chapter 4 there are cases where a better approximation can be reached by handling the Coulomb potential directly. The problem with the Coulomb potential classically is tunneling not being possible making a completely full classical model for HHG impossible and handling the Coulomb potential has to be done by hand. When we expanded the three step model for SPEAR NSDR HHG we added a single Coulomb interaction at some point relatively far from the emission point which enabled the electron to obtain enough momentum to simply traverse the Coulomb interaction and not recombine. This will not be true in general for smaller internuclear distances that we will study and a new approach will be needed.

We make two models: for small internuclear distances where we treat all interaction with the nuclei in the emission and recombination steps as being encompassed by the ionization potential and only let the electron interact with the bare nuclei when traversing the nuclei in the propagation step. For large internuclear distances we treat the second nuclei as a constant interaction and only treat the recombination and emission nuclei interaction as being included in the ionization potential. The transition point between the models will be determined from the HHG spectra. Using these models classical kinetic return energies are calculated by solving the equations of motion as described in chapter 4.

Using this expanded model on the non-exchange paths described in chapter 2 we find new cutoffs shown in fig. 5.1. Exchange paths will lead to similar behavior has seen in fig. 2.5 as the Coulomb potentials only perturb the classical results previously found. There are two branches present for each NSDR type because of the two nuclei in the system. Depending on the field direction one nuclei will be in front and one in behind compared to the direction an electron will be emitted in creating a difference between which core the electrons are emitted from. "1+2 Front" (full blue line) denotes the return kinetic

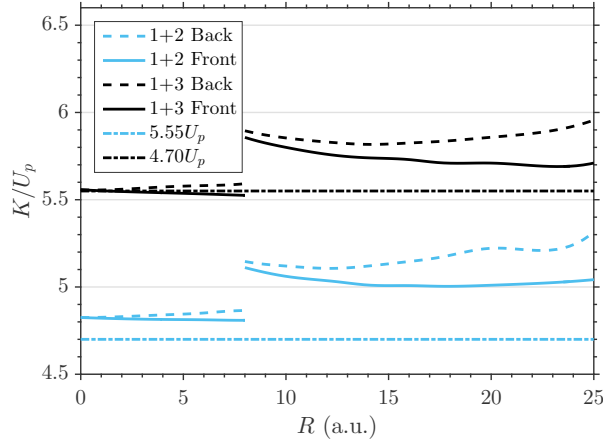


Figure 5.1: The kinetic return energies K in units of U_p as a function of the internuclear distance with a discontinuity at $R = 8.0$ between the two different models used. There are two branches for each type of NSDR HHG as depending on the field direction there will be one nuclei in front and another behind which creates a difference energetically in the kinetic return energy of an emitted electron. The discontinuity is experimentally set by what is observed in the spectra. See text for description of the models used. The atomic NSDR HHG cutoff energies presented in chapter 2 are plotted as references.

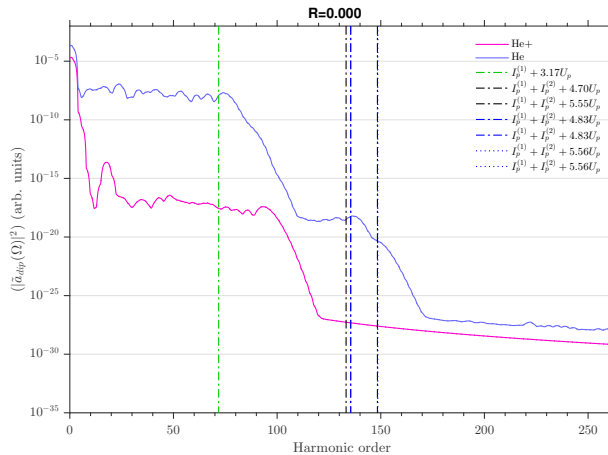


Figure 5.2: The smoothed HHG spectra for the He model. The spectra are shown in units of the Harmonic order for an $n = 15$ -cycle laser pulse at $\omega = 0.0584$ ($\lambda \simeq 780$ nm) and $F_0 = 0.119$ ($I \simeq 5.0 \times 10^{14}$ W/cm²). The HHG cutoffs for one electron HHG are shown as the dotted vertical lines in green at $I_p^{(1)} + 3.17U_p$. The two electron NSDR HHG cutoffs for the normal three-step model are the vertical black dotted lines at $I_p^{(1)} + I_p^{(2)} + 4.70U_p$ and $I_p^{(1)} + I_p^{(2)} + 5.55U_p$ and the enhanced three-step model are the vertical blue striped lines at $I_p^{(1)} + I_p^{(2)} + 4.83U_p$, $I_p^{(1)} + I_p^{(2)} + 4.83U_p$, $I_p^{(1)} + I_p^{(2)} + 5.56U_p$ and $I_p^{(1)} + I_p^{(2)} + 5.56U_p$.

energy of electrons where the first electron is emitted from the front nuclei and recombines at the second return. We observe that for small internuclear distances the difference between the front and back as it is expected when the spatial distance between the nuclei is small.

We have chosen a few molecular distances to highlight the molecular trends and effects that come (and go) as the intermolecular distance grows. The spectra are all smoothed for these long pulses to make it easier to identify cutoffs. The dipole acceleration spectrum for He is shown in Fig. 5.2. The (blue) curve extending to higher order in Fig. 5.2 is the full two electron model with correlation. There clearly are two plateaus where the first has a cutoff at $I_p^{(1)} + 3.17U_p$ which is what is expected classically for a pulse of this type. The second plateau located at $\Omega \approx [100\omega, 150\omega]$ has two cutoffs. This plateau is the

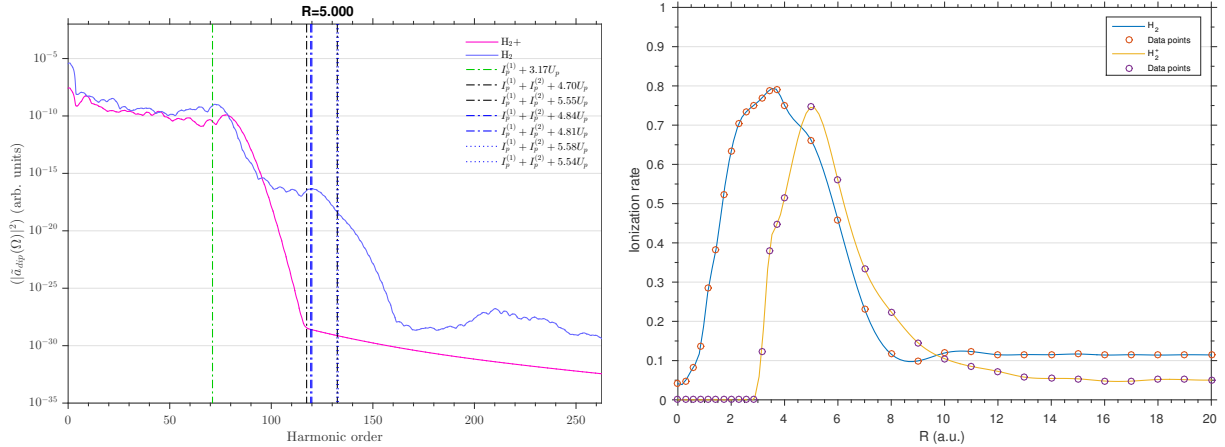


Figure 5.3: Fig. (a) is the HHG spectra for the H_2 model for $R = 5.0$. See caption of fig. 5.2 for explanation of legends. Fig. (b) is the ionization rate of H_2 and H_2^+ in after 6-cycles of the pulse as a function of the internuclear distance. The ionization rate is measured after 6-cycles to avoid total ionization for certain internuclear distances.

NSDR signal. The first cutoff is observed at $I_p^{(1)} + I_p^{(2)} + 4.83U_p$, which classically is a combination of maximum energy for an electron returning for the first time and an electron returning for the second time resulting in NSDR, and the second cutoff is observed at $I_p^{(1)} + I_p^{(2)} + 5.56U_p$ which classically is the maximum energy of an electron returning for the first time and an electron returning for the third. (See classical analysis in chapter 2 and fig. 5.1 for explanation of cutoffs). The one-electron models do of course not have the second plateau since NSDR is a two-electron effect. As is also seen in fig. 5.1 there is very little difference in the cutoffs from the normal three step model to the enhanced model we have introduced when looking at small internuclear distances. The 1+3 cutoff is practically the same as for the normal three step model but the difference for the 1+2 cutoff places the predicted cutoff exactly where we observe it in the spectrum. It is noted that such a precise agreement with the observed cutoff was not seen in the original paper predicting NSDR [18].

In Fig. 5.3 (a) the HHG spectrum for H_2 with $R = 5.0$ is shown. There is a rise in the NSDR signal for H_2 over the entire NSDR plateau located at $\Omega \approx [90\omega, 150\omega]$. This can be explained by the lowering of the ionization potential $I_p^{(2)}$ at $R = 5.0$ compared with $R = 0.0$ (see Fig. 3.1) which enhances the ionization rate as seen in fig. 5.3 (b). Here the ionization rate is defined as one subtracted by the norm of the wave function. This enhancement of the ionization rate leads to a greater amount of electrons in the continuum which can recombine as NSDR thereby increasing the amplitude of the NSDR signal. This enhancement of the NSDR is a molecular effect and this would be expected for all molecules with similar behavior of the ionization potential with R . It is noted that the pulse intensity could be revised to maximize the NSDR HHG signal for each internuclear distance but for ease of comparison between the different internuclear distances one universal pulse is used for all. Enhancing the NSDR HHG signal for all internuclear distances will be addressed in chapter 6. It is also again noted that the enhanced three-step model is better at predicting the cutoff of the 1+2 NSDR HHG but as seen in fig. 5.1 not much difference is expected between the enhanced model and the simple three-step model.

In fig. 5.4 the HHG spectra for $R = 8.0$ and $R = 9.0$ is presented. A shift in the cutoffs of NSDR HHG is detected at this point. For the used molecular model a shift in the electron dynamics happen at this point. The two-electron ground state has one electron on each nuclei so when the first electron tunnels out from one nuclei the second will be localized on the other nuclei. For small internuclear

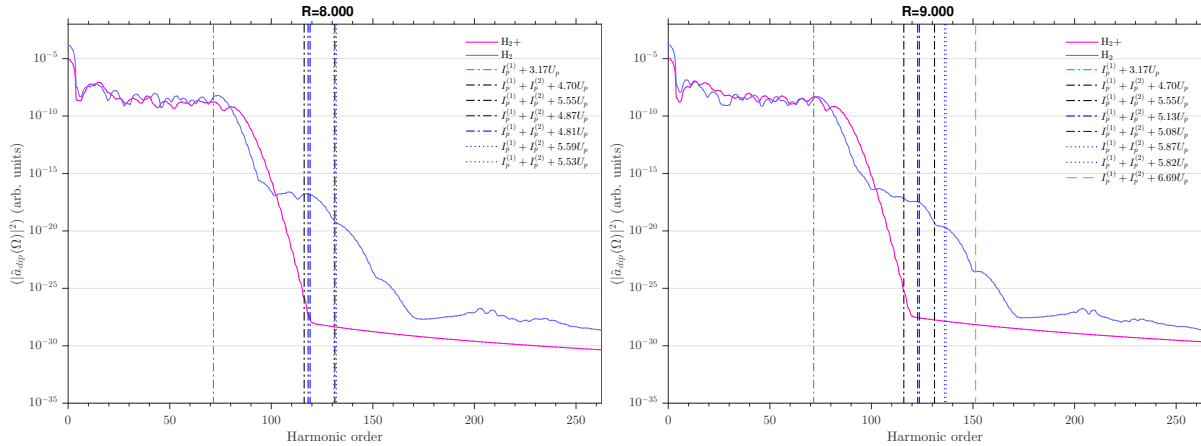


Figure 5.4: The HHG spectra for the H_2 model for $R = 8.0$ in fig. (a) and $R = 9.0$ in fig. (b). See caption of fig. 5.2 for explanation of legends. There is a shift in the cutoffs from $R = 8.0$ to $R = 9.0$ as the bound electrons no longer are able to oscillate between nuclei when the other tunnels out.

distances the electron still bound in the molecule will be able to oscillate between the two nuclei as the potential barrier between will be low. From $R = 8.0$ to $R = 9.0$ the barrier becomes so large the electron is unable to oscillate and the two nuclei therefore become separate entities changing the model needed to describe the system. From this it is then expected that the NSDR HHG cutoffs will behave like almost like the atomic system as the only difference is the small difference in location of the nuclei compared to the quiver length in the field when the electron traverses the nuclei. To further study this transition from the oscillatory internuclear distances to non-oscillatory we have done one-electron TDSE calculations where the one-electron ground state is found with only the Coulomb interaction from one nuclei. We then introduce the Coulomb interaction from the second nuclei in a real time propagation to emulate the two-electron system after one electron is emitted. We find that the system reproduces the behavior described with the wave function oscillating between the nuclei when $R \leq 8.0$. The physical significance of this transition also comes when considering ionization where the nuclei of origin is of relevance. Observing the spectra in fig. 5.4 (b) we see that the lowest energy branch for 1+2 and 1+3 cutoff in NSDR HHG is located at the cutoffs observed in the spectrum. From this we can conclude that the location where emission of electrons is most likely is the front nuclei compared to the field direction. Importantly for the proposed models to describe NSDR HHG in molecules the cutoffs change significantly for $R = 9.0$ as seen in fig. 5.4 (b) and the model predicts them perfectly.

In Fig. 5.5 (a) the HHG spectrum for H_2 with $R = 16.0$ is given. The two distinct cutoffs from "1+2" and "1+3" NSDR HHG cutoffs seen in previous spectra are now gone and we now see a continuous fall in signal from $I_p^{(1)} + I_p^{(2)} + 5.01U_p$ till $I_p^{(1)} + I_p^{(2)} + 5.83U_p$ where a cutoff is observed. We ascribe this behavior to molecular effects of exchange paths. The one-electron system has a relatively flat plateau until the classically maximal energy is reached where after the signal falls until the NSDR HHG signal becomes measurable. What happens in the fall of seen in the NSDR HHG signal is instead a variety of less likely processes of higher and higher energy contributing creating a less pronounced fall in signal compared to the cutoff seen after the one-electron plateau. The molecular exchange paths can obtain more energy when propagating as seen in fig. 2.5 but are less likely to happen. This After $I_p^{(1)} + I_p^{(2)} + 5.83U_p$ the signal again falls until a new signal becomes measurable again. This new cutoff is the SPEAR NSDR HHG signal that has risen in amplitude when compared to fig. 5.4 (b).

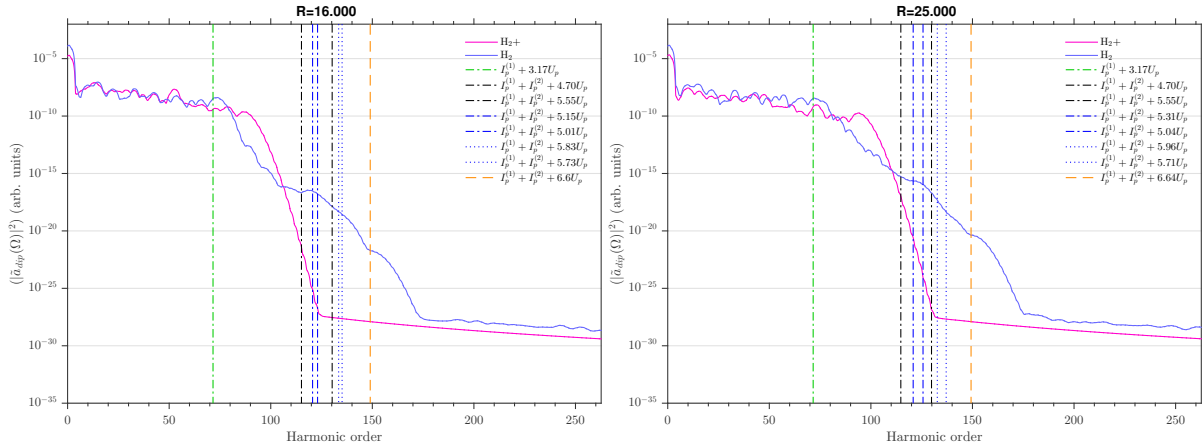


Figure 5.5: The HHG spectra for the H_2 model for $R = 16.0$ in fig. (a) and for $R = 25.0$ in fig. (b). See caption of fig. 5.2 for explanation of legends.

Figure 5.5 (b) shows the HHG spectrum for H_2 with $R = 25.0$. This is the limit for the internuclear distance for which direct paths from the one-electron signal does not drown the NSDR HHG signal. The direct paths can be seen in the H_2^+ HHG signal as the difference between the cutoff of the H_2 cutoff at $I_p^{(1)} + 3.17U_p$ to the observed H_2^+ cutoff at around 95ω . The observed behavior of the NSDR HHG signal seen in fig. 5.5 (a) is retained with $I_p^{(1)} + I_p^{(2)} + 5.04U_p$ marking the start of the fall in signal until the cutoff at $I_p^{(1)} + I_p^{(2)} + 5.96U_p$. The ability of our models to correctly mark cutoffs in the NSDR HHG signal for internuclear distances up-to $R = 25.0$ signifies they describe the behavior of the NSDR HHG process well even though they are a classical description of an advanced quantum mechanical phenomenon. It is also noted that the $I_p^{(1)} + I_p^{(2)} + 5.96U_p$ cutoff is not fitting well anymore supporting our claim that the molecular exchange paths widen the NSDR HHG cutoffs as this would be the expected behavior when the internuclear distance increases.

5.1 Summary

Using the knowledge gained from identifying SPEAR NSDR HHG in chapter 4 we proposed two models to describe NSDR HHG in molecular systems. We found that these models work in two different regimes defined by the charge transfer dynamics in the molecular system. For large internuclear distance we see the predicted molecular dynamics proposed in chapter 2 but no distinct structures are observed because of these effects. From the models it would seem we have a solid grasp of the dynamics involved in NSDR HHG.

Using this it would be of interest to use attosecond pulses to control these dynamics and maybe make NSDR HHG easier to measure as the low NSDR signal strength compared to the one-electron signal will be a problem experimentally.

We will mention that the proposed classical model is a relatively small perturbation on the simple three step model proposed originally for atomic NSDR HHG and we have in the model ignored other know effects in ionization through tunneling [19]. Non-zero velocity after tunneling and emission points different from exactly on the nuclei have been tested and make little difference for the cutoff energies and they have therefore been ignored in the model to only introduce the interactions needed to explain the observed HHG spectra.

6 Attosecond Pulse Enhancement of Non-sequential Double Recombination High Harmonic Generation

The previous chapters was a study of the HHG signal emitted from a system after a single femtosecond pulse had interacted with it. The goal was to understand the process of NSDR HHG in a molecular system and produce theory capable of explaining the structures seen in the HHG signal and thereby understanding the underlying process. Using the knowledge obtained about the NSDR HHG process from the classical model we will now try to control and enhance the NSDR HHG signal through interactions with attosecond pulses. This is an ongoing project and we will here present preliminary results.

Previous studies have used pulse modeling to create specialized pulses that enhance the signal from HHG [28]. We are going to limit our selves to attosecond pulses and use our knowledge about the classical process to control ionization in the HHG process. Such schemes have been used by others to enhance and study electron dynamics [29, 30]. For all systems studied the NSDR signal was several orders of magnitude lower than what was seen for the one-electron HHG signal. As shown in chapter 2 the process of non-SPEAR NSDR HHG is a combination of a long paths traversing the nuclei of the atom or molecule multiple times and an electron returning for the first time. The time window in a pulse cycle where long HHG paths are emitted from the nuclei is very small which significantly halts the signal of NSDR HHG to rise. When comparing the HHG spectra for Helium in chapter 4 and 5 we observe an increase in the NSDR HHG signal in the long pulse case. This can be explained by the enhanced ionization rate for the long pulse compared with the 6-cycle pulse. We can therefore conclude that an enhancement of the ionization rate will increase the NSDR signal, as was seen in fig. 5.3 (a). Increasing the field strength would be an option for some systems but the limit of complete ionization will limit this option.

We instead aim to emit electrons at the times in the pulse we know NSDR HHG paths are created. Attosecond pulses are very short XUV pulses of down to a single cycle with a pulse width of 67as [31]. We will use a single cycle pulse width a pulse frequency of $\omega_{atto} = 0.88$ to create a one-photon transition from the two-electron ground state in Helium to one electron in the continuum and the other bound in the Helium ion. The frequency is set beneath the ionization potential of helium to avoid above threshold ionization as much as possible [32]. The pulse form used is:

$$F(t) = -\frac{\partial A(t)}{\partial t} = \frac{F_{0,atto}}{\omega_{atto}} \exp \left[-4 \ln 2 \frac{(t - t_{atto})^2}{FWHM^2} \right] \times \cos[\omega_{atto}(t - t_{atto})], \quad (6.1)$$

where $F_{0,atto}$ is the attosecond pulse field strength, t_{atto} is when the attosecond pulse interacts with the system and $FWHM$ is the full-width-half-max of resulting in a pulse width being $4 \ln 2 / FWHM^2$. We use $F_{0,atto} = 0.1$ in our calculations and with $\omega_{atto} = 0.88$ a one-cycle pulse has a width of 3.5 a.u. = 85 as. This is the theoretical minimum of a attosecond pulse width the chosen frequency.

We have made calculations for a semi-long pulse with $n = 6$ but using the pulse form in eq. 3.4 for a range of t_{atto} in the first period of the flat part of the envelope of the field. HHG yields have in the literature been increased using attosecond pulse trains but this is not possible for NSDR HHG as the disturbance of multiple attosecond pulses is bigger in amplitude than the NSDR HHG signal [33].

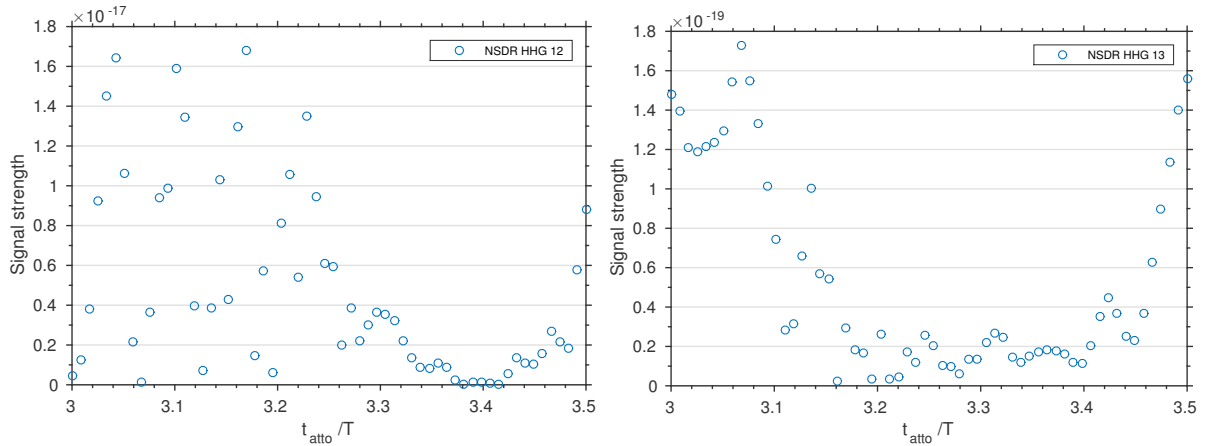


Figure 6.1: The signal strength of the HHG signal at the NSDR cutoffs "1+2" in fig. (a) and "1+3" in fig. (b) as a function of the time the attosecond pulse interacts with the system.

The signal as a function of the time the attosecond pulse interacts with the systems can be seen in fig. 6.1. We have chosen to plot the signal at the frequency of the "1+2" cutoff for the atomic system in fig. 6.1 (a) and as a function of the "1+3" cutoff in fig. 6.1 (b). We expect that the NSDR HHG signal would be enhanced when the attosecond pulse ionizes the system at the start of the period. It is at these times the long paths are emitted. This behavior is seen in fig. 6.1 (b) but it is harder to distinguish in fig. 6.1 (a). From the classical model we would expect the "1+3" signal to be enhanced for only a narrow band of time as the more returns the electrons have, the narrower the window of emission from the nuclei, but even the "1+3" enhancement is larger than what would be expected if total control was obtainable with the attosecond pulse. We must therefore conclude that the width of the attosecond pulse might be too wide to have total control of the NSDR HHG process but even with these problems a significant rise in the signal is observed, even though we are using a relatively long pulse reducing the problem of missing ionization.

6.1 Further Study

The work with attosecond pulses is ongoing and there are several options for further investigation. If an even larger amount of control would be had from the interaction with the attosecond pulse, we could make calculations with larger wavelength which hopefully would reduce the effect of the attosecond pulse on the system and maybe making the usage of an attosecond pulse train possible. Together with a longer wavelength a lower field strength could be used for the femtosecond pulse, reducing the amount of ionization coming from the interaction with the femtosecond pulse. This would be comparable to the method used for attosecond streaking which was mentioned in the introduction. Using few-cycle femtosecond pulses as in chapter 4 could also be of interest as a distinct single cycle is responsible for emitting the long path electrons that recombine into NSDR later for the maximum cutoff frequency. We could therefore choose if we want to enhance the "1+2" NSDR HHG signal or the "1+3" NSDR HHG signal.

7 Outlook

In this report I have presented my work on NSDR HHG done until this point in my PhD. In chapter 2 I presented a classical perspective on HHG and proposed molecular paths relevant for two electron HHG. In chapter 3 I present the computational methods used to solve the TDSE for two electrons in a reduced dimensionality model. In chapter 4 I present a new NSDR HHG process that had not previously been documented and the new model we developed to explain the signal observed. This new process was published in [1] and presented at the multiphoton conference in Andover, New Hampshire in June 2016. The new model had significant importance when extended to general NSDR HHG and was extended for the general case of molecular NSDR HHG in chapter 5. The developed model predicts two different regimes of the NSDR HHG process which was found in chapter 5 to be dependent on charge transfer in the molecular model used. Using these models we are able to find effects of the molecular structure on the HHG spectrum and make precise predictions about the structure of the NSDR HHG spectrum. Finally in chapter 6 we present the preliminary work done with attosecond pulses to enhance the NSDR HHG signal and control the NSDR process to gain further knowledge about the NSDR process. Through this study of NSDR HHG I have acquired knowledge of the complications in solving multi-electron systems and the different approaches possible for such problems. I have looked into the tools normally used in the field of ultra science such as SFA even though the work bore no fruit in regards to NSDR HHG. The work on molecular NSDR HHG in chapter 5 is planned to be summed up into a publication in the future as the final part of this study of NSDR HHG.

Future work will be directed towards a study abroad in Rostock, Germany. We have started talks with Dr. Dieter Bauer at the University of Rostock, whose group work with density matrix functional theory and natural orbitals applied to few-electron strong-field processes and coulomb-corrected quantum orbits and other subjects closely laying to the project of NSDR HHG. As the previous project is nearing its end this opens an opportunity for diversification into a new subject in collaboration with Dr. Bauer even though nothing precise has been discussed as of turning in this report.

Bibliography

- [1] Kenneth K. Hansen and Lars Bojer Madsen. Same-period emission and recombination in nonsequential double-recombination high-order-harmonic generation. *Phys. Rev. A*, 93:053427, May 2016.
- [2] R. M. Potvliege C. J. Joachain, N. J. Kylstra. *Atoms in Intense Laser Fields*. Cambridge University Press, University Printing House, Cambridge CB2 8BS, United Kingdom, 1 edition, 7 2014.
- [3] P. B. Corkum. Plasma perspective on strong field multiphoton ionization. *Phys. Rev. Lett.*, 71:1994–1997, Sep 1993.
- [4] M. Lewenstein, Ph. Balcou, M. Yu. Ivanov, Anne L’Huillier, and P. B. Corkum. Theory of high-harmonic generation by low-frequency laser fields. *Phys. Rev. A*, 49:2117–2132, Mar 1994.
- [5] B. Walker, B. Sheehy, L. F. DiMauro, P. Agostini, K. J. Schafer, and K. C. Kulander. Precision measurement of strong field double ionization of helium. *Phys. Rev. Lett.*, 73:1227–1230, Aug 1994.
- [6] GrgurasI., MaierA R., BehrensC., MazzaT., KellyT J., RadcliffeP., DustererS., KazanskyA K., KabachnikN M., TschentscherTh., CostelloJ T., MeyerM., HoffmannM C., SchlarbH., and CavalieriA L. Ultrafast x-ray pulse characterization at free-electron lasers. *Nat Photon*, 6(12):852–857, Dec 2012.
- [7] Extreme light infrastructure. <http://www.eli-np.ro/>. Accessed: 2016-08-12.
- [8] Ferenc Krausz and Misha Ivanov. Attosecond physics. *Rev. Mod. Phys.*, 81:163–234, Feb 2009.
- [9] Michael G. Pullen, Benjamin Wolter, Anh-Thu Le, Matthias Baudisch, Michael Hemmer, Arne Senftleben, Claus Dieter Schroter, Joachim Ullrich, Robert Moshhammer, C. D. Lin, and Jens Biegert. Imaging an aligned polyatomic molecule with laser-induced electron diffraction. *Nat Commun*, 6, Jun 2015. Article.
- [10] R. Torres, N. Kajumba, Jonathan G. Underwood, J. S. Robinson, S. Baker, J. W. G. Tisch, R. de Nalda, W. A. Bryan, R. Velotta, C. Altucci, I. C. E. Turcu, and J. P. Marangos. Probing orbital structure of polyatomic molecules by high-order harmonic generation. *Phys. Rev. Lett.*, 98:203007, May 2007.
- [11] Wen Li, Xibin Zhou, Robynne Lock, Serguei Patchkovskii, Albert Stolow, Henry C. Kapteyn, and Margaret M. Murnane. Time-resolved dynamics in n2o4 probed using high harmonic generation. *Science*, 322(5905):1207–1211, 2008.
- [12] Jeffrey L. Krause, Kenneth J. Schafer, and Kenneth C. Kulander. High-order harmonic generation from atoms and ions in the high intensity regime. *Phys. Rev. Lett.*, 68:3535–3538, Jun 1992.
- [13] M. Lein, N. Hay, R. Velotta, J. P. Marangos, and P. L. Knight. Interference effects in high-order harmonic generation with molecules. *Phys. Rev. A*, 66:023805, Aug 2002.
- [14] Jérôme Levesque, Yann Mairesse, Nirit Dudovich, Henri Pépin, Jean-Claude Kieffer, P. B. Corkum, and D. M. Villeneuve. Polarization state of high-order harmonic emission from aligned molecules. *Phys. Rev. Lett.*, 99:243001, Dec 2007.
- [15] Xibin Zhou, Robynne Lock, Nick Wagner, Wen Li, Henry C. Kapteyn, and Margaret M. Murnane. Elliptically polarized high-order harmonic emission from molecules in linearly polarized laser fields. *Phys. Rev. Lett.*, 102:073902, Feb 2009.
- [16] A. D. Bandrauk, S. Chelkowski, H. Yu, and E. Constant. Enhanced harmonic generation in extended molecular systems by two-color excitation. *Phys. Rev. A*, 56:R2537–R2540, Oct 1997.
- [17] Manfred Lein and Jan M. Rost. Ultrahigh harmonics from laser-assisted ion-atom collisions. *Phys. Rev. Lett.*, 91:243901, Dec 2003.
- [18] P. Koval, F. Wilken, D. Bauer, and C. H. Keitel. Nonsequential double recombination in intense laser fields. *Phys. Rev. Lett.*, 98:043904, Jan 2007.
- [19] Misha Ivanov and Olga Smirnova. How accurate is the attosecond streak camera? *Phys. Rev. Lett.*, 107:213605, Nov 2011.
- [20] Thomas Brabec. *Strong Field Laser Physics*, volume 134. Springer-Verlag New York, 2009.
- [21] Jeppe Olsen Trygve Helgaker, Poul Jorgensen. *Molecular Electronic-Structure Theory*. Wiley, 2000.

- [22] Haruhide Miyagi and Lars Bojer Madsen. Time-dependent restricted-active-space self-consistent-field theory for laser-driven many-electron dynamics. *Phys. Rev. A*, 87:062511, Jun 2013.
- [23] H. G. Muller. An efficient propagation scheme for the time-dependent schrödinger equation in the velocity gauge. *Laser Physics*, 9(1):138–148, 1990.
- [24] K. Burnett, V. C. Reed, J. Cooper, and P. L. Knight. Calculation of the background emitted during high-harmonic generation. *Phys. Rev. A*, 45:3347–3349, Mar 1992.
- [25] Yong-Chang Han and Lars Bojer Madsen. Comparison between length and velocity gauges in quantum simulations of high-order harmonic generation. *Phys. Rev. A*, 81:063430, Jun 2010.
- [26] Albert H. Nuttall. Some windows with very good sidelobe behavior. *Acoustics, Speech and Signal Processing, IEEE Transactions on*, 29(1):84–91, Feb 1981.
- [27] J M Dahlström, A L’Huillier, and A Maquet. Introduction to attosecond delays in photoionization. *Journal of Physics B: Atomic, Molecular and Optical Physics*, 45(18):183001, 2012.
- [28] R. Bartels, S. Backus, E. Zeek, L. Misoguti, G. Vdovin, I. P. Christov, M. M. Murnane, and H. C. Kapteyn. Shaped-pulse optimization of coherent emission of high-harmonic soft x-rays. *Nature*, 406(6792):164–166, Jul 2000.
- [29] Andre D. Bandrauk and Nguyen Hong Shon. Attosecond control of ionization and high-order harmonic generation in molecules. *Phys. Rev. A*, 66:031401, Sep 2002.
- [30] A. C. Brown and H. W. van der Hart. Extreme-ultraviolet-initiated high-order harmonic generation: Driving inner-valence electrons using below-threshold-energy extreme-ultraviolet light. *Phys. Rev. Lett.*, 117:093201, Aug 2016.
- [31] Kun Zhao, Qi Zhang, Michael Chini, Yi Wu, Xiaowei Wang, and Zenghu Chang. Tailoring a 67 attosecond pulse through advantageous phase-mismatch. *Opt. Lett.*, 37(18):3891–3893, Sep 2012.
- [32] D B Milošević, G G Paulus, D Bauer, and W Becker. Above-threshold ionization by few-cycle pulses. *Journal of Physics B: Atomic, Molecular and Optical Physics*, 39(14):R203, 2006.
- [33] Mette B. Gaarde, Kenneth J. Schafer, Arne Heinrich, Jens Biegert, and Ursula Keller. Large enhancement of macroscopic yield in attosecond pulse train–assisted harmonic generation. *Phys. Rev. A*, 72:013411, Jul 2005.